Journal of Power Sources 185 (2008) 1386–1391

Contents lists available at ScienceDirect

Journal of Power Sources

journal homepage: www.elsevier.com/locate/jpowsour

# Electrochemical behaviour of tin borophosphate negative electrodes for energy storage systems

Atef Y. Shenouda [a,*], Hua Kun Liu [b]

[a] Central Metallurgical Research and Development Institute (CMRDI), Tebbin, Helwan, Helwan, Egypt
[b] Institute for Superconducting and Electronic Materials, ARC Centre of Excellence for Electromaterials Science, University of Wollongong, NSW 2522, Australia

ARTICLE INFO

*Article history:*
Received 3 July 2008
Received in revised form 12 August 2008
Accepted 16 August 2008
Available online 27 August 2008

*Keywords:*
Lithium battery negative electrode
Tin borophosphate electrode
Antimony doping

ABSTRACT

Tin borophosphate compounds doped with antimony, $Sn_2BP_{1-x}Sb_xO_6$ ($x$ = 0–0.3), have been prepared and studied by X-ray diffraction (XRD), scanning electron microscopy (SEM), Fourier transmission infrared spectroscopy (FTIR), electrochemical impedance spectroscopy (EIS), and cyclic voltammetry (CV) and galvanostatic measurements. XRD patterns of all the samples were indexed to the tetragonal system. The EIS showed that the conductivities are enhanced by antimony doping. It was observed that the Warburg impedance coefficient ($\sigma_w$) was 1163.265 $\Omega\,cm^2\,s^{-0.5}$ for the $Sn_2BP_{0.9}Sb_{0.1}O_6$ ($x$ = 0.1) sample, and this was the lowest value compared to those of the other samples. $Sn_2BP_{0.9}Sb_{0.1}O_6$ ($x$ = 0.1) showed the highest specific discharge capacity of 1050 mAh $g^{-1}$ among all the samples and a reversible capacity of 540 mAh $g^{-1}$ at the 150th cycle.



## 1. Introduction

Tin oxide compounds (TOC) have been suggested as high capacity anode materials for lithium-ion batteries [1,2]. Their rechargeability is based on the reversibility in the electrochemical reactions involving structurally related phases of Li–Sn alloys [3]. The alloy phase is believed to be dispersed in an oxide matrix consisting primarily of the decomposition products formed during the first Li intercalation reaction. The most notable deficiencies of tin oxide compounds are their irreversible capacity loss in the first charge cycle and their poor cyclability relative to carbon-based anodes. The TOC that delivers the best electrochemical performance is reported with $SnB_{0.56}P_{0.40}Al_{0.42}O_{0.36}$ composition [4]. The synthesis of this compound is difficult because of the high melting point of the $Al_2O_3$ raw material, necessitating processing temperatures as high as 1100 °C. Special equipment and care are also needed to reduce the evaporative loss of volatile components such as $B_2O_3$ and $P_2O_5$. In this investigation, $BPO_4$ was used instead to reduce the volatility problem of $B_2O_3$ and $P_2O_5$. $BPO_4$ reacts with SnO at elevated temperatures to form $Sn_2BPO_6$, which was used as a model TOC anode in rechargeable lithium test cells. Its electrochemical performance is comparable with those of $Sn_2B_2O_5$ and $Sn_2P_2O_7$, which are TOCs with only one glass formation promoter (B or P). There has been a resurgence of interest in the use of lithium-alloy anodes because of their low first cycle capacity losses [5]. Most recent implementations have addressed the major deficiency of bulk alloys (material fragmentation consequent upon the large volume changes in intercalation and de-intercalation) by dispersing the active material as ultra-fine particles in a suitable matrix [6–8]. The matrix is often an inactive phase, but an active host material may also be used [9]. The effectiveness of this approach is determined by the ability of the matrix to restrain the particle growth of the active phase. It is in this latter category that TOCs may still hold an edge over the multiphase alloy systems.

Three tin compounds, namely $Sn_2P_2O_7$, $Sn_2B_2O_5$, and $Sn_2BPO_6$, have been prepared by melt-quenching the appropriate reaction mixtures [10]. The borate glass was the easiest to form, but it was visually the least homogeneous and delivered the poorest electrochemical performance. Hence, the amount of B in any glassy TOC should be carefully controlled to reach a balance between the ease of synthesis and electrochemical performance.

Although similar alloying and de-alloying mechanisms were involved in charge and discharge reactions, $Sn_2P_2O_7$ and $Sn_2BPO_6$ cycled much better than $Sn_2B_2O_5$ at the current density of 20 mA $g^{-1}$. When the cells were cycled at higher current and a higher discharge potential limit (150 mA $g^{-1}$ and 1.4 V, respectively), $Sn_2BPO_6$ displayed the best capacity retention relative to $Sn_2P_2O_7$ and $Sn_2B_2O_5$. This is perhaps due to the robustness of the $BPO_6^{4-}$ structure in charge and discharge reactions.

The major advantage of TOC over carbonaceous anodes is their large specific capacities on either the gravimetric or volumetric basis. They are, however, hampered by the large irreversible

* Corresponding author. Tel.: +20 25010642; fax: +20 25010639.
*E-mail address:* ayshenouda@yahoo.com (A.Y. Shenouda).

0378-7753/$ – see front matter © 2008 Elsevier B.V. All rights reserved.
doi:10.1016/j.jpowsour.2008.08.042

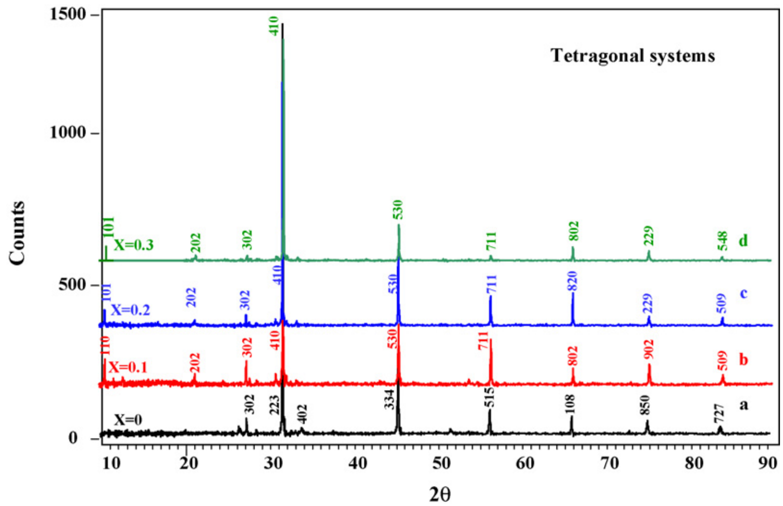


**Fig. 1.** XRD patterns of $Sn_2BP_{1-x}Sb_xO_6$ samples.

capacity loss in the first cycle. A promising solution is perhaps to disperse tin particles in an ionically and electronically conducting medium. The medium should also contain a mechanism to dissipate the mechanical stress induced by the large volume change in alloying and de-alloying reactions. The use of multiphase alloys and composites containing nanosize active and inactive components are the basis of some demonstrated experiments [11]. In addition, new chemistries such as those based on Al and Sb composites are also being explored for lithium-ion applications [12,13].

Tin dioxide- and antimony-doped tin dioxide thin films were prepared by using a sol–gel technique [14]. The films were homogeneous in composition and morphology, and showed a remarkable decrease in the grain size (down to a few nanometers) and resistivity when doped with antimony. Films were tested as potential anodes in lithium-ion batteries. The best electrochemical performance was obtained from the $Li/SnO_2$ with 5 wt% Sb, which provided more than 250 mAh $g^{-1}$ during 75 cycles, while the $Li/SnO_2$ cell capacity faded after a few cycles. Good electrochemical behaviour of the doped systems in comparison to the un-doped ones was discussed in terms of their mechanical and electronic properties.

In this work, the doping of antimony into $Sn_2BPO_6$ was used to improve the cyclability and reversible capacity of this electrode material, due to its effects on the crystal structure and grain size.

## 2. Experimental

### 2.1. Materials preparation

Samples of composition: $Sn_2BP_{1-x}Sb_xO_6$, where $x$ = 0, 0.1, 0.2, and 0.3, were prepared from stoichiometric amounts of $SnCl_2 \cdot 2H_2O$ (Alfa Aesar), $NH_4H_2PO_4$ (Polarabo), and $H_3BO_3$ (CDH) dissolved in distilled water. $Sb_2O_3$ (Aldrich) was dissolved in $HNO_3$ separately, and after that the raw material compounds were mixed together. Citric acid was added in double molarity with respect to the total molar ratio of the dissolved precursor compounds. The mixed solution was stirred and heated until a gel was formed. The combustion of the organic materials took place at 250 °C. The fired samples were calcined at 750 °C for 12 h in an alumina crucible, and calcination was repeated for another 12 h at the same temperature. The final prepared samples were labeled as a, b, c, and d corresponding to $x$ = 0, 0.1, 0.2, and 0.3, respectively.

### 2.2. Materials characterisations

Powder X-ray diffraction (XRD) measurements were carried using a Philips Powder diffractometer with Cu Kα radiation. Infrared absorption spectra were recorded using a Nicolet Avatar 360 Fourier Transform Infrared Spectrophotometer. Samples were ground to fine powders, mixed and diluted with KBr. They were then vacuum pressed into translucent disks. The IR region examined was 400–4000 $cm^{-1}$. Elemental compositions of the various tin oxide composites were analysed by inductively coupled plasma (ICP, PerkinElmer Optima 2000 DV). Scanning electron microscopy (SEM) was conducted with a JEOL SEM Model 6460.

### 2.3. Electrochemical measurement

The homogeneous slurry used to form the electrodes was composed of 80 wt% active materials, 12 wt% acetylene black and 8 wt% polyvinylidene fluoride (PVDF) binder dissolved in *N*-methyl pyrrolidone (NMP) solvent. It was then spread onto Ni foam (1 mm thickness) substrates. The area of each coated electrode was 1 $cm^2$. The electrodes were dried in a vacuum oven under a vacuum pressure of 30 Torr at 110 °C for 12 h. The electrodes were then pressed at a pressure of 2000 kg $cm^{-2}$. The active material loading was about 4 mg for each individual electrode. Stainless steel coin cells were then assembled in an argon filled glove box (Mbraun, Unilab, Germany) using lithium metal foil as the counter electrode. The electrolyte was 1 M $LiPF_6$ in a mixture of ethylene carbonate (EC) and dimethyl carbonate (DMC) (1:1, v/v, provided by MERCK). The cells were galvanostatically charged and discharged over a voltage range of 0.1–2 V using current of 0.02 A for both processes. Cyclic voltammetry (CV) measurements were performed using a Multistat CHI660 Electrochemical Workstation at a 0.1 mV $s^{-1}$ scanning rate and the potential windows were 0 and 2 V vs. $Li/Li^+$ electrode. The AC impedance measurement amplitude was 50 mV. The frequency range was 100 kHz–10 mHz.

## 3. Results and discussion

The X-ray diffraction patterns of $Sn_2BP_{1-x}Sb_xO_6$ are shown in Fig. 1. Samples diffraction peaks exhibited well-defined crystal structures. Their structures were indexed to the tetragonal system using software program (Tracers V6) with the XRD patterns. The refined unit cell parameters are given in Table 1. The existence of

**Table 1**
Unit cell parameters of tetragonal $Sn_2BP_{1-x}Sb_xO_6$ compounds

| No. | Sample composition amount of $x$ | $a$ (Å) | $c$ (Å) | Cell volume, $V$ (Å$^3$) | FWHM (°) at $2\theta$ = 31.7° | Crystallite size, $D$ (nm) |
|---|---|---|---|---|---|---|
| a | $x$ = 0.0 | 11.6028 | 11.3563 | 1607.58 | 0.102 | 80.97518 |
| b | $x$ = 0.1 | 11.8979 | 11.925 | 1605.4 | 0.0816 | 101.2274 |
| c | $x$ = 0.2 | 11.6175 | 11.923 | 1609.2 | 0.102 | 80.96496 |
| d | $x$ = 0.3 | 11.587 | 11.914 | 1599.6 | 0.122 | 67.69868 |

$SbPO_4$ was observed at 21.66° (1 1 0) as explained by ICDD card no. 35-829. The crystal structure data of $SbPO_4$ were reported by Santos Pen et al. [15]. The crystallite size $D$ was approximated from the X-ray line width, $w$, at full width at half maximum (FWHM) according to the Scherer formula, $D = 0.9\lambda/w\cos\theta$ where $\lambda$ is the X-ray wavelength (1.5406 Å) and $\theta$ is the diffraction angle [16]. It was found that $w$ (FWHM) increased with the increase of $Sb^{5+}$ concentration as reported by Bernardi et al. [17]. The previous formula gives crystallite size $D$ = 101.22 nm for sample "b" that is the greatest value in comparison with the other samples ones. It was reported that antimony ($Sb^{5+}$) doping decreases the unit cell parameters ($a$, $c$) and consequently the crystallite size according to its ionic radius (0.74 Å) while $Sb^{3+}$ (0.90 Å) increases those ones [18]. The ionic radius for the six coordinated $Sn^{4+}$ is 0.83 Å. Such behaviour of the cell parameters may indicate that both $Sb^{3+}$ and $Sb^{5+}$ ions were substituted for $Sn^{4+}$ in the samples with variable $Sb^{3+}$/ $Sb^{5+}$ content ratio. This probably indicates that sample "b" has more $Sb^{3+}$ than $Sb^{5+}$ ions.

Fig. 2 shows SEM images of $SnBP_{1-x}Sb_xO_6$. The powders have average crystal sizes between 6 and 12 μm. The doping with antimony at low concentration modifies and decreases the grain size, which has likewise been reported in the literature [14,19]. It was reported that the small grain size does not allow for tin atoms to form large clusters [18]. As clusters grow in size, they cause the material to fail for the same reasons as for bulk Li–Sn alloys, i.e. disintegration and loss of electrical contact. Therefore, doping with a small amount of antimony may have the ability to keep the tin dispersed, despite extensive cycling.

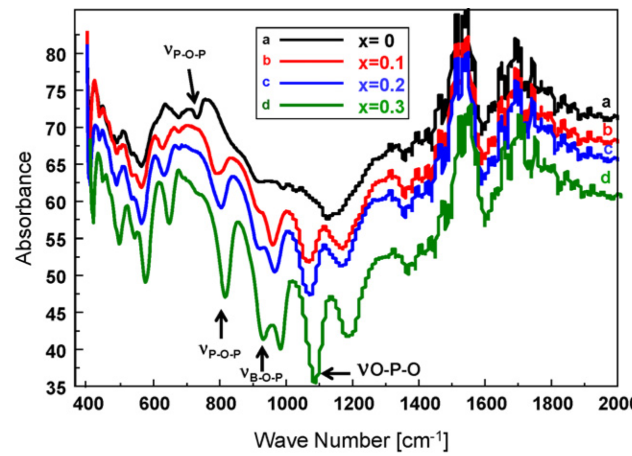


**Fig. 3.** FTIR spectra of $Sn_2BP_{1-x}Sb_xO_6$ samples; $x$ = 0–0.3.

In Fig. 3, FTIR spectra show νP–O–P, νB–O–P and νO–P–O at 800, 930, and 1070 cm$^{-1}$, respectively. The band at 750 cm$^{-1}$ corresponds to the P–O–P stretch vibration between two $PO_4$ tetrahedra [10,20]. The peaks at 1070 cm$^{-1}$ correspond to the O–P–O vibration within the $PO_4$ tetrahedron. It is observed that the P–O–P peak is shifted towards higher wave number by the addition of antimony, and it reaches 820 cm$^{-1}$ for sample "d". The connection between the phosphate units is affected by the incorporation of antimony in

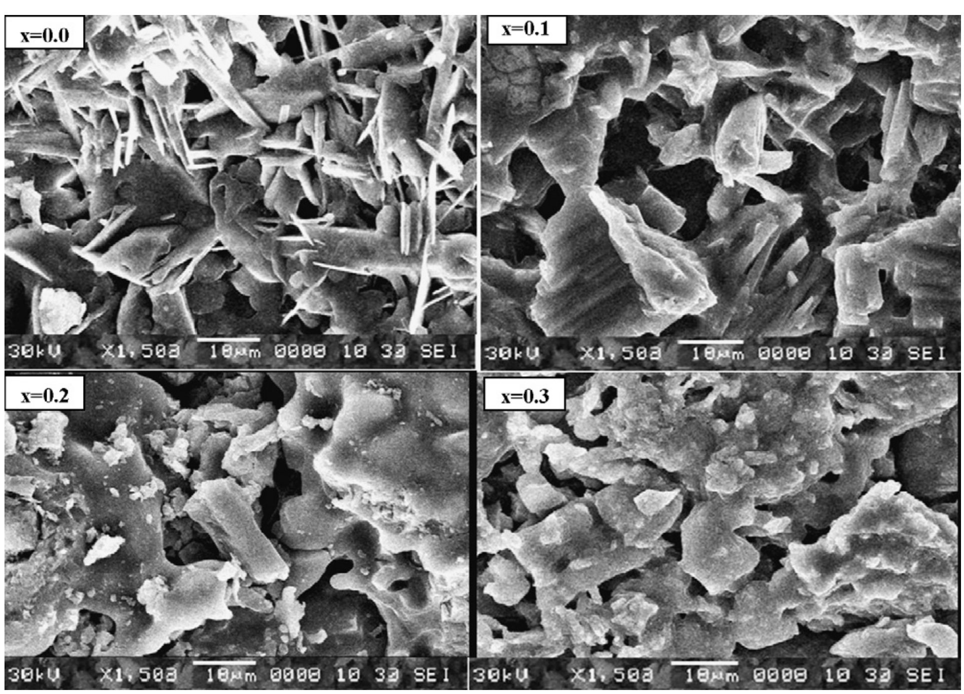


**Fig. 2.** SEM images of $Sn_2BP_{1-x}Sb_xO_6$ samples; $x$ = 0–0.3.

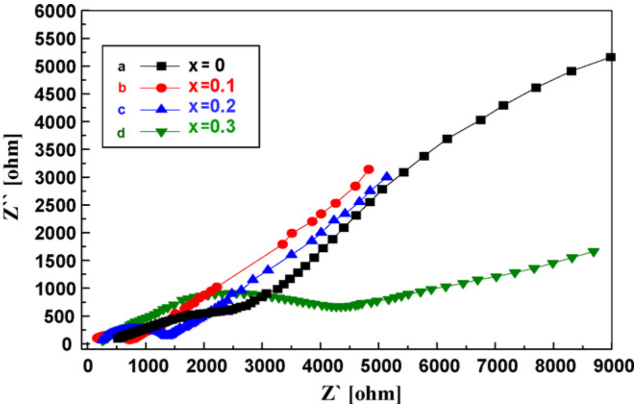


**Fig. 4.** EIS of $Li/Sn_2BP_{1-x}Sb_xO_6$ cells: (a) $x = 0$; (b) $x = 0.1$; (c) $x = 0.2$; and (d) $x = 0.3$.

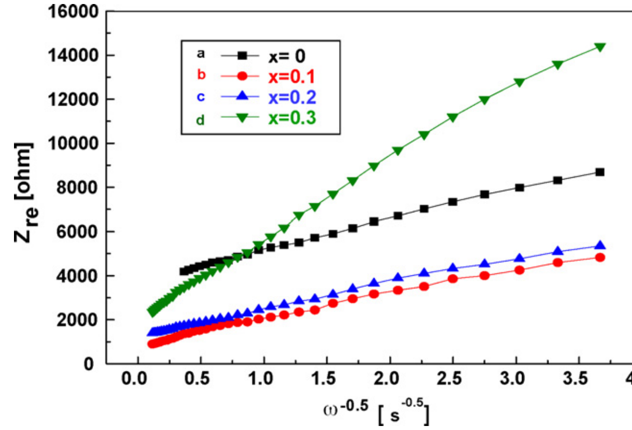


**Fig. 5.** Relationship between real impedance with the low frequencies for $Li/Sn_2BP_{1-x}Sb_xO_6$ cells: (a) $x = 0$; (b) $x = 0.1$; (c) $x = 0.2$; and (d) $x = 0.3$.

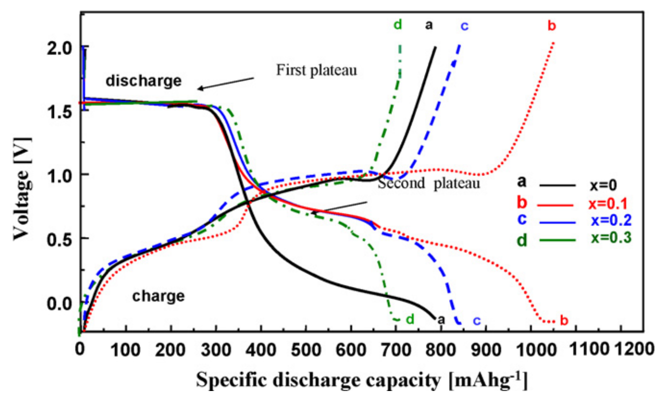


**Fig. 6.** Voltage profiles vs. first specific charge–discharge capacities for $Li/Sn_2BP_{1-x}Sb_xO_6$ cells: (a) $x = 0$; (b) $x = 0.1$; (c) $x = 0.2$; and (d) $x = 0.3$. The charging–discharging currents are $20\,mA\,cm^{-2}$.

addition to the tin and boron incorporation. Tin and antimony will occupy some of the positions usually taken up by phosphorous in the glass network and form $SbSnO_{3,4}$-units. The peak at $930\,cm^{-1}$ is attributed to the B–O–P vibration within $BPO_4$. So, there is a possibility that the borate groups are more spread out along the chains consisting of $PO_4$- and $SnO_{3,4}$-groups.

The electrochemical impedance spectra of the cells as illustrated in Fig. 4 show an intercept at high frequency for the resistance of the electrolyte, $R_e$ on the real axis $Z_{re}$ , followed by a semicircle in the high-middle frequency region, and a straight line in the low frequency region. The numerical value of the diameter of the semicircle on the $Z_{re}$ axis is approximately equal to the charge transfer resistance, $R_{ct}$, therefore, it can be seen that there is a marked decrease in $R_{ct}$ after doping. The low frequency region of the straight line is attributed to the diffusion of the lithium ions into the bulk of the electrode material, the so-called Warburg diffusion.

In fact, electrochemical impedance spectroscopy (EIS) may be considered as one of the most sensitive tools for the study of differences in the electrode behaviour due to surface modification. The plot of the $Z_{re}$ vs. the reciprocal square root of the lower angular frequencies is illustrated in Fig. 5. The straight lines are attributed to the diffusion of the lithium ions into the bulk of the electrode materials, the so-called Warburg diffusion. This relation is governed by Eq. (1). It is observed that the Warburg impedance coefficient ($\sigma_w$) is $1163.265\,\Omega\,cm^2\,s^{-0.5}$ for sample "b", and this is the lowest value in comparison with those of the other samples. Also, the diffusion coefficient values of the lithium ions in the bulk electrode materials are calculated using Eq. (2) and recorded in Table 2. Also, the parameters of the equivalent circuit are recorded in Table 2:

$$Z_{re} = R_e + R_{ct} + \sigma_w \omega^{-0.5} \tag{1}$$

$$D = 0.5\left(\frac{RT}{AF^2\sigma_w C}\right)^2 \tag{2}$$

where $R_{ct}$, charge transfer resistance; $R_e$, electrolyte resistance; $\omega$, angular frequency in the low frequency region, $D$, diffusion coefficient; $R$, the gas constant; $T$, the absolute temperature; $F$, Faraday's constant; $A$, the area of the electrode surface; and $C$, molar concentration of $Li^+$ ions (moles $cm^{-3}$) [21].

The obtained diffusion coefficient ($2.62 \times 10^{-14}\,cm^2\,s^{-1}$) for cell "b" explains the higher mobility for $Li^+$ ion diffusion in this cell rather than the other cells. Furthermore, the exchange current density ($i^\circ = RT/nFR_{ct}$) of cell "b" is higher than for the other cells. Therefore, the charge-transfer reaction is stronger in the $Sn_2BP_{0.9}Sb_{0.1}O_6$ electrode than in the other electrodes.

The first discharge capacity plateaus vs. the working voltage between 2 and 0.0 V are shown in Fig. 6. The profiles for the first reduction look fairly similar for all the samples. There are two plateaus at about 1.7 and 0.8 V vs. $Li^+$ for cells "b–d" that are attributed to the reduction of $Sn^{4+}$ to metallic Sn(0) and the formation of lithium–antimony alloys, respectively [15]. The first discharge curve of cell "b" delivers the highest specific discharge capacity of about $1050\,mAh\,g^{-1}$. Similar results were observed in the literature [10,14]. The other voltage profiles for charge–discharge curves until 30 cycles of cell "b" are explained in Fig. 7.

Cyclic voltammetry (CV) experiments as shown in Fig. 8(a) and (b) were performed between 2 and 0.0 V vs. $Li^+/Li$ at a scan

**Table 2**
The impedance parameters of $Sn_2BP_{1-x}Sb_xO_6$ cells

| No. | $x$ value in $Sn_2BP_{1-x}Sb_xO_6$ | $R_e$ ($\Omega$) | $R_{ct}$ (() | $\sigma$ ($\Omega\,cm^2\,s^{-0.5}$) | $D$ ($cm^2\,s^{-1}$) | $i^\circ$ ($mA\,cm^{-2}$) |
|---|---|---|---|---|---|---|
| a | 0 | 259 | 3.47E+03 | 1443.878 | 1.70E-14 | 7.39E-06 |
| b | 0.1 | 167 | 7.87E+02 | 1163.265 | 2.62E-14 | 3.26E-05 |
| c | 0.2 | 253 | 9.93E+02 | 1234.694 | 2.32E-14 | 2.59E-05 |
| d | 0.3 | 521 | 4.25E+03 | 3653.061 | 2.65E-15 | 6.04E-06 |

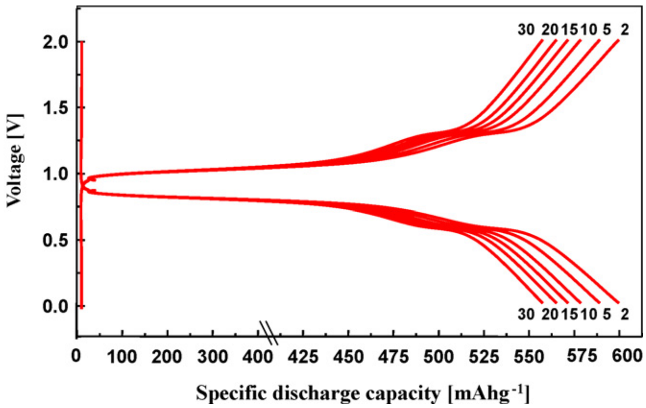


**Fig. 7.** Voltage profiles for Li/$Sn_2BP_{0.9}Sb_{0.1}O_6$ ($x$ = 0.1) cell. The charging and discharging currents are 20 mA $cm^{-2}$.

rate of 0.1 mV $s^{-1}$. The CV of cell "a" has two cathodic reduction plateaus and one anodic plateau. The first reduction peak for all the four materials is represented by an irreversible peak at around 1.68 V. This peak could be suggested to the reaction between $Sn_2BP_{1-x}Sb_xO_6$ and lithium according to:

$$Sn_2BP_{1-x}Sb_xO_6 + 4Li \rightarrow 2Sn + xSb + Li_4BP_{1-x}O_6 \quad (3)$$

$$Sn + xSb \rightarrow SnSb_x \quad (4)$$

Therefore the reaction between lithium and $Sn_2BP_{1-x}Sb_xO_6$ is not an intercalation reaction, but one that destroys the network as reported by Santos Pena et al. [15]. The second reduction peak for cell "a" observed at 0.25 V is attributed to lithium alloying with tin to yield several $Li_xSn$ compounds ($1 \le x \le 4.4$) as follows [19,14,22]:

$$Sn + xLi^+ + xe \rightarrow Li_xSn \quad (5)$$

The reduction peak observed for cells "b–d" at 0.8–085 V (second plateau in Fig. 6(a)) can be analysed in comparison with that reported for antimony intermetallics [15,19,23]. Antimony particles formed during the first plateau can further react with lithium yield $Li_3Sb$ according to:

$$Sb + 3Li \rightarrow Li_3Sb \quad (6)$$

The additional cycles of cell "b" are recorded in Fig. 9. These cyclic voltammograms have similar plateaus of the anodic and cathodic peaks.

The lithium extraction from these alloys is indicated in the oxidation profile by the presence of a peak at 0.5 V. The de-alloying reaction of lithium with antimony occurs at around 1–1.15 V, which is observed for the doped samples. The mechanism of lithium insertion in the tin oxide base materials can be categorically described as follows: at low levels of Li insertion, the Sn–O active centres in TOC react with intercalating Li to give rise to microscopically dispersed $Li_2O$ and metallic Sn (β-Sn mostly). At increasing levels of Li insertion, the metallic Sn alloys with lithium to form various Li–Sn alloys with a maximum stoichiometry of $Li_{4.4}Sn$. The presence of Li–Sn alloys was reported and verified by XRD [24], Mössbauer spectroscopy [25] and nuclear magnetic resonance (NMR) [26].

Fig. 10 illustrates the specific discharge cyclic performance of the different cells. Each cell was charged and discharged at 0.02 A between 2 and 0.01 V at room temperature. It is clearly observed that the reversible specific discharge capacity has shown some decrease from the initial cycling stage. The initial discharge capacity is due to the reduction of $Sn_2PBO_6$ and $Sn_2BP_{1-x}Sb_xO_6$ to Sn and $SnSb_x$, respectively, beside $Li^+$ to Li(0). This capacity translates to 6.2 equiv. mol of Li ions per mole of Sn in the alloy $Li_xSn$ [2,10]. The low efficiency of the discharge capacity is caused by the irreversible reaction between lithium and $Sn_2PBO_6$ to form metallic tin, which could then be used to store and release $Li^+$, and after this the reversible capacity returns to about 550 mAh $g^{-1}$ for cell "b" (4 mol of Li per mole of tin). Cell "b" shows a reversible capacity decrease of 10% from about 600 to 540 mAh $g^{-1}$ after 150 cycles. The other cells show a similar decrease in their discharge capacities with cycling, but their specific discharge capacities are smaller than those of cell "b".

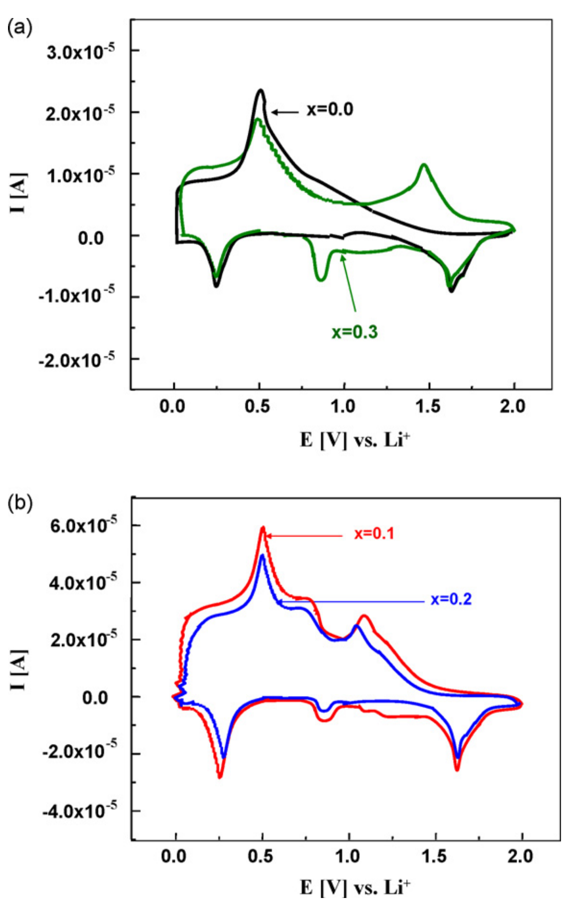


**Fig. 8.** First CVs of Li/$Sn_2BP_{1-x}Sb_xO_6$ cells: (a) for $x$ = 0.0, and 0.3 (b) for $x$ = 0.1 and 0.2, scan rate $10^{-4}$ V $s^{-1}$.

The high and good reversible capacity of sample "b", $Sn_2BP_{0.9}Sb_{0.1}O_6$, is attributed to the low formation of aggregated

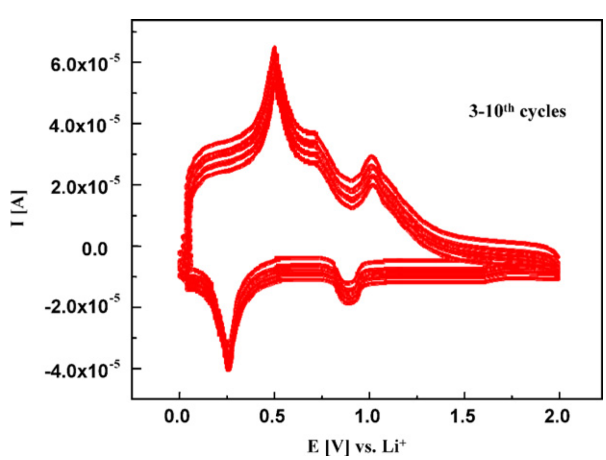


**Fig. 9.** CVs of Li/$Sn_2BP_{0.9}Sb_{0.1}O_6$ ($x$ = 0.1) cell, scan rate $10^{-4}$ V $s^{-1}$.

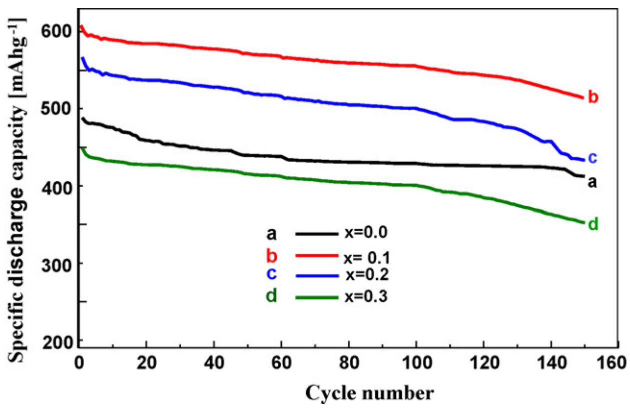


**Fig. 10.** Specific discharge capacities vs. cycle number for Li/$Sn_2BP_{1-x}Sb_xO_6$ cells: (a) $x = 0$; (b) $x = 0.1$; (c) $x = 0.2$; and (d) $x = 0.3$. The charging and discharging currents are 20 mA $cm^{-2}$.

tin atoms (clusters). This is due to the small grain size and higher surface area of this sample, as observed in the XRD and SEM investigations. However, tin-based materials undergo severe structural and volume changes during the inserting and removal of $Li^+$. This greatly limits the mechanical stability and cycle life of the electrode.

## 4. Conclusion

The powders have average crystal sizes between 6 and 12 μm, while sample "b", with $x = 0.1$ ($SnBP_{0.9}Sb_{0.1}O_6$), has a small average size of about 1–2 μm. Therefore, sample "b" exhibits a small particle size and a consequent large surface area. The doping with antimony at a particular concentration modifies the grain size. There is a possibility that the borate groups are more spread out along the chains consisting of $PO_4$- and $SnO_{3,4}$-groups. Cell "b" shows a reversible capacity decrease of 10% from about 600 to 540 mAh $g^{-1}$ after 150 cycles. The high and good reversible capacity of sample "b", $Sn_2BP_{0.9}Sb_{0.1}O_6$, is attributed to the low formation of aggregated tin atoms. This is due to the small grain size of this sample, which does not allow for tin atoms to form large clusters. As clusters grow in size, they cause the material to fail for the same reasons as for bulk Li–Sn alloys, i.e. disintegration and loss of electrical contact. Therefore, doping with a small amount of antimony has the ability to keep the tin dispersed, despite extensive cycling.

## Acknowledgments

Financial support provided by the Australian Research Council (ARC) through ARC Centre of Excellence funding (CE0561616) is gratefully acknowledged. Also authors thank Dr. Tania Silver at the University of Wollongong for critical reading of the manuscript. Also, Dr. Atef Shenouda would like to thank the Egyptian Ministry of Higher Education and Scientific Research for supporting him the postdoctoral fellowship grant that he carried out this research in ISEM, University of Wollongong.

## References

[1] J.H. Ahn, G.X. Wang, J. Yao, H.K. Liu, S.X. Dou, J. Power Sources 119–121 (2003) 45.
[2] I.A. Courtney, J.R. Dahn, J. Electrochem. Soc. 144 (1997) 2045.
[3] Y. Idota, Y. Miyaki, T. Kubota, T. Miyasaka, European Patent 0,651,450 A1 (1994).
[4] J.O. Besenhard, J. Yang, M. Winter, J. Power Sources 68 (1997) 87.
[5] R.A. Higgins, in: J.O. Besenhard (Ed.), Handbook of Battery Materials, Wiley-VCH, Weinheim, Germany, 1998, p. 359.
[6] J. Yang, M. Wachtler, M. Winter, J.O. Besenhard, Electrochem. Solid State Lett. 2 (1999) 161.
[7] O. Mao, J.R. Dahn, J. Electrochem. Soc. 146 (1999) 423.
[8] K.D. Kepler, J.T. Vaughey, M.M. Thackeray, Electrochem. Solid State Lett. 2 (1999) 307.
[9] J.Y. Lee, R. Zhang, Z. Liu, Electrochem. Solid State Lett. 3 (2000) 167.
[10] J.Y. Lee, Y. Xiao, Z. Liu, Solid State Ionics 133 (2000) 25.
[11] Y. Liang, J. Fan, X. Xia, Z. Jia, Mater. Lett. 61 (2007) 4370.
[12] C.M. Ionica, P.E. Lippens, J.O. Fourcade, J.C. Jumas, J. Power Sources 146 (2005) 478.
[13] M.-Z. Xue, Z.-W. Fu, Electrochem. Commun. 8 (2006) 1250.
[14] J.S. Peña, T. Brousse, L. Sánchez, J. Morales, D.M. Schleich, J. Power Sources 97–98 (2001) 232.
[15] J. Santos Pen, J.C. Pascual, A. Caballero, J. Morales, L. Sanchez, J. Solid State Chem. 177 (2004) 2920.
[16] S.R.S. Prabaharan, A. Fauzi, M.S. Michael, K.M. Begam, Solid State Ionics 171 (2004) 157.
[17] M.I.B. Bernardi, L.E. Soledade, I.A. Santo, E.R. Leite, E. Longo, J.A. Varela, Thin Solid Films 405 (2002) 228.
[18] B. Gržeta, E. Tkalčec, C. Goebbert, M. Takeda, M. Takahashi, K. Nomura, M. Jakšić, J. Phys. Chem. Solids 63 (2002) 765.
[19] H. Zhao, C. Yin, H. Guo, J. He, W. Qiu, Y. Li, J. Power Sources 174 (2007) 916.
[20] C. Gejke, E. Zanghellini, L. BoÈrjesson, L. Fransson, K. EdstroÈm, J. Phys. Chem. Solids 62 (2001) 1213.
[21] A.J. Bard, L.R. Faulkner, Electrochemical Methods, second ed., John Wiley & Sons, New York, 2001, p. 231.
[22] Z. Wang, W. Tian, X. Li, J. Alloys Compd. 439 (2007) 350.
[23] L. Simonin, U. Lafont, N. Tabrizi, A. Schmidt-Ott, E.M. Kelder, J. Power Sources 174 (2007) 805.
[24] I.A. Courtney, W.R. McKinnon, J.R. Dahn, J. Electrochem. Soc. 146 (1999) 59.
[25] A. Hightower, P. Delcroix, G. Le Caer, C.K. Huang, B.V. Ratnakumar, C.C. Ahn, B. Fultz, J. Electrochem. Soc. 147 (2000) 1.
[26] Y. Wang, J. Sakamoto, C.K. Juang, S. Surampudi, S.G. Greenbaum, Solid State Ionics 110 (1998) 167.